MATERIALS SCIENCE

Resonant nanodiffraction x-ray imaging reveals role of magnetic domains in complex oxide spin caloritronics

Paul G. Evans[1]*, Samuel D. Marks[1], Stephan Geprägs[2], Maxim Dietlein[2,3], Yves Joly[4], Minyi Dai[1], Jiamian Hu[1], Laurence Bouchenoire[5,6], Paul B. J. Thompson[5,6], Tobias U. Schülli[7], Marie-Ingrid Richard[7,8], Rudolf Gross[2,3,9], Dina Carbone[10], Danny Mannix[4,11,12]

Copyright © 2020 The Authors, some rights reserved; exclusive licensee American Association for the Advancement of Science. No claim to original U.S. Government Works. Distributed under a Creative Commons Attribution NonCommercial License 4.0 (CC BY-NC).

Spin electronic devices based on crystalline oxide layers with nanoscale thicknesses involve complex structural and magnetic phenomena, including magnetic domains and the coupling of the magnetism to elastic and plastic crystallographic distortion. The magnetism of buried nanoscale layers has a substantial impact on spincaloritronic devices incorporating garnets and other oxides exhibiting the spin Seebeck effect (SSE). Synchrotron hard x-ray nanobeam diffraction techniques combine structural, elemental, and magnetic sensitivity and allow the magnetic domain configuration and structural distortion to be probed in buried layers simultaneously. Resonant scattering at the Gd L_2 edge of $Gd_3Fe_5O_{12}$ layers yields magnetic contrast with both linear and circular incident x-ray polarization. Domain patterns facet to form low-energy domain wall orientations but also are coupled to elastic features linked to epitaxial growth. Nanobeam magnetic diffraction images reveal diverse magnetic microstructure within emerging SSE materials and a strong coupling of the magnetism to crystallographic distortion.

INTRODUCTION

Developments in the field of spin electronics promise to extend its scope far beyond the original vision of applications in computing and information technologies. In spintronic materials and devices, the coupling of the charge and spin degrees of freedom led to applications such as giant magnetoresistance transducers and spin-transfer torque oscillators (*1*, *2*). Recent discoveries have shown that an even far broader scope of applications can be accessed by the coupling of spin, charge, and heat currents in one and the same material. One particularly promising extension of spintronic phenomena is in thermoelectric generation, broadly termed spin caloritronics (*3*). If optimized, thermoelectric technologies can enable the direct conversion of thermal energy to electrical power (*4*). In conventional thermoelectrics, an electric current is generated by a temperature gradient. For efficient devices, good electrical and poor thermal conductivity is required, vastly complicating the design of materials and devices (*5*, *6*). Spin caloritronics provides a complementary novel approach based on the spin Seebeck effect (SSE). Here, a spin current is driven by a temperature gradient in a magnetic insulator (MI) with thermal transport properties far better suited to device applications (*3*, *7*–*9*). This article reports the discovery of a diverse magnetic microstructure within emerging SSE materials and of a strong coupling of the magnetic structure to crystallographic distortion. A novel synchrotron hard x-ray resonant nanobeam diffraction method and a new magnetic contrast imaging mechanism provide combined structural and elemental specificity, uniquely allowing precise magnetic and structural information to be obtained simultaneously from nanoscale buried volumes. Advanced x-ray methods resolve longstanding uncertainties in the nanoscale magnetism and structure of the single-crystalline magnetic materials and, when combined with advances in synthesis and lithography, will enable new horizons in spin caloritronics and spintronic devices more generally.

The SSE is typically based on the development of a spin current in an MI as a result of a temperature gradient. This spin current is injected into an adjacent high–atomic number metal (HM) and transformed into an electrical (charge) current via the inverse spin Hall effect, transducing the thermal gradient to an electrical current (*8*). The physics of SSE devices is currently described by a model in which thermopower in MI/HM bilayers results from magnonic spin currents (*8*, *9*). Furthermore, the optimization of SSE devices in zero magnetic field requires a precise knowledge of the magnetic microstructure of the MI and the correlation between this magnetic microstructure and the generated voltage. In particular, in the absence of an external magnetic field, magnetic inhomogeneity arising from the three-dimensional distribution of magnetic domains can strongly influence the magnon propagation and therefore the spin current at the MI/HM interface and consequently degrade the thermoelectric efficiency (*8*, *10*). The magnetic domain configuration is also affected by strain imposed by the substrate used to template the epitaxial growth of the MI, crystallographic and chemical defects, and the attached conducting HM layer in ways that are not yet known.

Here, we report the discovery of the zero–magnetic field domain configuration within the garnet $Gd_3Fe_5O_{12}$ (GdIG), a prototypical SSE material for which the chemical and magnetic structure appears in Fig. 1A (*4*, *11*). The thinness, nanoscale domain dimensions, and magnetic complexity of the magnetic garnet layers pose challenges for magneto-optical characterization (e.g., second-harmonic generation and magneto-optical imaging and coupled optical/SSE measurements) (*8*, *12*), polarized neutron reflectivity (*13*), photoemission

[1]University of Wisconsin-Madison, Madison, WI 53706, USA. [2]Walther-Meißner-Institut, Bayerische Akademie der Wissenschaften, 85748 Garching, Germany. [3]Physik-Department, Technische Universität München, 85748 Garching, Germany. [4]Université Grenoble Alpes, CNRS, Institut Néel, 38042 Grenoble, France. [5]XMaS, ESRF, The European Synchrotron, 38043 Grenoble, France. [6]University of Liverpool, Department of Physics, Liverpool L69 3BX, UK. [7]ESRF, The European Synchrotron, 38043 Grenoble, France. [8]Aix Marseille Université, CNRS, IM2NP UMR 7334, Université de Toulon, Marseille 13397, France. [9]Munich Center for Quantum Science and Technology (MCQST), Schellingstraße 7, 80799 München, Germany. [10]MAX IV Laboratory, Fotongatan 2, 224 84 Lund, Sweden. [11]European Spallation Source, SE-221 00 Lund, Sweden. [12]Aarhus University, Langelandsgade 140, DK-8000 Aarhus, Denmark.
*Corresponding author. Email: pgevans@wisc.edu

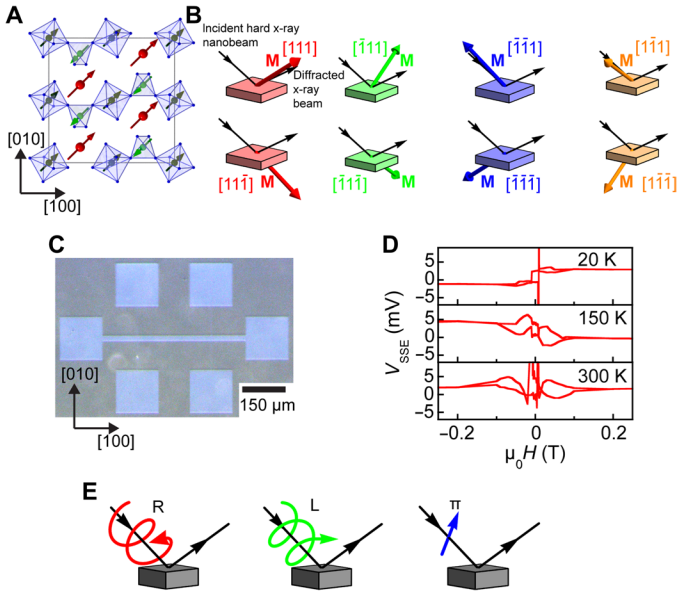

Fig. 1. Magnetic structure of GdIG. (**A**) Atomic structure and magnetic moments in one atomic layer of the GdIG cubic unit cell, highlighting oxygen octahedra and tetrahedra. Arrows indicate the directions of the magnetic moments of Gd^{3+} ions (red) and Fe ions on tetragonal (light green) and octahedral (dark green) sites. (**B**) Directions of the total magnetization **M** under the assumption of bulk-like ⟨111⟩ magnetization directions in a (001)-oriented GdIG thin film. (**C**) Hall bar SSE device consisting of a patterned GdIG MI and a thin Pt conductor. (**D**) Magnetic field hysteresis of V_{SSE} at 20, 150, and 300 K. (**E**) Electric field polarization vectors for right (R)–, left (L)–, and π-polarized incident x-ray nanobeams.

microscopy (*14*), and magnetic force microscopy (*15*). As a result, magnetic microscopy methods have probed domains near surfaces or in bulk crystals or thick epitaxial layers relevant to magneto-optics rather than in the nanoscale buried layers of spin caloritronic devices (*16*, *17*). Hard x-ray nanodiffraction, as described here, however, uses photon energies of several kilo–electron volts or more and couples both to the magnetism and the crystallographic nanoscale structure, providing a unique combination of layer, site, and element specificity. The development of this hard x-ray ferromagnetic imaging approach extends previous imaging of ferromagnetic and antiferromagnetic materials (*15*, *18*–*21*) by providing structural and magnetic sensitivity simultaneously.

X-ray nanobeam maps obtained for a GdIG thin film with thickness $\Delta = 21$ nm using beamline ID01 at the European Synchrotron Radiation Facility indicate that the magnetic domain morphology has a critical impact on the efficiency of the SSE voltage generation in devices based on GdIG. Structural features such as strain and nanoscale morphology appear to be related to the magnetic domain morphology and provide the means to control the domain pattern and thus optimize devices.

Thick (111)-oriented GdIG layers have domains of out-of-plane magnetization with alternating direction, separated by Bloch domain walls above about 190 K (*15*, *22*, *23*). Comparatively little experimental or theoretical insight is available into the complex magnetic configuration that can be expected in (001)-oriented nanoscale layers in zero magnetic field due to the competition among effects arising from nanoscale geometry, elastic distortion, and magnetic anisotropy (*15*, *16*, *24*–*26*). Possible directions of magnetization within a magnetic domain in (001)-oriented GdIG are illustrated in Fig. 1B, under the assumption that the net magnetization of GdIG is along magnetically easy bulk ⟨111⟩ directions. There remains, however, significant uncertainty regarding the direction of magnetization in GdIG ultrathin layers due to shape anisotropy and magnetoelastic effects. In part, the uncertainty arises because of the lack of local nanoscale characterization that promises to be resolved by the x-ray methods presented in this article. The analysis presented below uses the bulk magnetic polarization as a guide to interpreting results, but the possibility that shape anisotropy leads to in-plane magnetization in ultrathin garnet layers remains open.

RESULTS

The lithographically patterned SSE Hall bar structure shown in Fig. 1C consists of GdIG ridges capped by an HM layer consisting of a 2.8-nm-thick Pt film. A thermal gradient through the thickness of the GdIG/Pt bilayer is generated by applying a current in the Pt layer. The SSE voltage V_{SSE} is measured in a perpendicular in-plane direction using a set of lateral electrical contacts (see Materials and Methods). For magnetic fields larger than the magnetic saturation field $\mu_0 H_{sf} \approx 0.2$ T, the sign of V_{SSE} switches when the external magnetic field $\mu_0\mathbf{H}$ (and therefore the overall magnetization **M** of the GdIG layer) is reversed. A further sign change of V_{SSE} as a function of temperature is obvious from Fig. 1D, which can be attributed to a competition of different magnon branches in GdIG (see Materials and Methods) (*4*, *11*). At lower magnetic fields, V_{SSE} has low–magnetic field hysteresis, which can be ascribed to changes of the magnetic domain structure in the GdIG thin film (Fig. 1D). V_{SSE} can be expected to be maximized when the MI exhibits single magnetic domain state, with **M** perpendicular to both the temperature gradient and the direction along which the voltage is measured. We infer, therefore, that the hysteresis in V_{SSE} is an experimental signature of the mesoscale reconfiguration of the magnetic domain pattern in the presence of the applied magnetic field (*27*). Understanding and controlling the zero-field magnetic domain direction in the MI layer thus become a defining, but previously unexploited, aspect of the design of SSE devices.

Maps of the magnetic domain structure within the GdIG layer covered by a thin Pt thin film without an applied magnetic field were obtained by combining synchrotron x-ray nanodiffraction with x-ray resonant magnetic scattering (XRMS). XRMS uses precise control of the incident x-ray polarization and yields a diffracted intensity that depends on the magnetization (*28*). Three relevant settings of the incident polarization are illustrated in Fig. 1E: circular polarizations with left (*L*) and right (*R*) helicity and linear polarization in the x-ray scattering plane, termed π polarization. As demonstrated below, using these three polarizations allows the scattering contrast between magnetic domains to be distinguished from the scattering arising from the atomic structure. Experiments were conducted using the magnetic sensitivity of the L_2 resonance of the Gd ions within the GdIG layer using photon energies near 7.94 keV. We therefore probe the magnetic domain structure of the magnetic Gd sublattice. The nanobeam measurements were conducted using an x-ray beam focused to a full width at half maximum (FWHM) spot size of 200 nm with the sample at a temperature of 5 K, at which the Gd^{3+} ions have a large saturated magnetization. The structure factor at the (008)–x-ray reflection weights all 12 Gd^{3+} ions in the structural unit cell equally and includes a negligible nonresonant x-ray magnetic scattering contribution from Fe^{3+} ions (*29*). Further experimental details are shown in Materials and Methods.

Magnetic information can be extracted from the diffracted x-ray intensity using flipping ratios, precisely defined normalized differences between intensities recorded with different incident polarizations. We use two flipping ratios closely linked to the magnetism of the Gd^{3+} ions: (i) F_{cir}, measured with opposite incident beam helicities and generally used in imaging approaches based on magnetic dichroism in absorption; and (ii) F_π, the normalized difference between intensities measured with π-polarized and the purely charged scattering component, which we introduce here. F_{cir} is familiar from x-ray scattering studies conducted using radiation scattered nearly parallel to the incident beam. π polarization is useful at large angles between the incident and diffracted beams, e.g., those of Bragg reflections. π polarization does not, however, provide magnetic contrast for small scattering angles and thus has not been considered in previous studies using only absorption contrast (*30*).

The flipping ratios are defined in terms of the diffracted x-ray intensities I_L, I_R, and I_π measured with left-, right-, and π-polarized incident beams as $F_{cir} = \frac{I_L - I_R}{2(I_L + I_R)}$ and $F_\pi = \frac{I_\pi - \alpha(I_L + I_R)}{\beta(I_L + I_R)}$. The factors $\alpha = \frac{\cos^2 2\theta}{1 + \cos^2 2\theta}$ and $\beta = \frac{2}{1 + \cos^2 2\theta}$ describe the polarization dependence of the scattering of linearly polarized light and depend on the Bragg angle θ. The sum $I_L + I_R$ yields purely structural information, which allows comparison of the crystallographic and magnetic structures. The circular flipping ratio F_{cir} can be expected to have maxima when the magnetization of the Gd sublattice lies in the scattering plane defined by the incident and diffracted x-ray beams (*28*). Similarly, F_π can be expected to reach a maximum when the magnetization is perpendicular to the scattering plane (*28*). These initial assumptions are consistent with more complete calculations using the finite-difference method for near edge structure (FDMNES) package (*31*).

Key features of the structure and magnetism of the GdIG layer at low temperature are revealed in Fig. 2 in x-ray nanobeam maps of a lithographically defined square around which the surrounding GdIG thin film was removed. An optical micrograph of this region appears in Fig. 2A. Maps of the flipping ratios F_{cir} and F_π in Fig. 2 (B and C) show the distribution of magnetic domains within the GdIG layer. The point-to-point variation of F_{cir} and F_π in Fig. 2 (B and C) is on the order of 1% and exhibits complementary contrast between the two flipping ratios that is distinct from the intensity variation in the structural image. As expected, no magnetic contrast is obtained in maps acquired with linear polarization in the plane of the surface, termed σ polarization (see plot in the Supplementary Materials). We focus now on the F_{cir} signal, which has a larger magnitude than F_π and which is thus readily amenable to further analysis.

The resonant character of the magnetic contrast was probed by repeating the nanobeam mapping at several x-ray photon energies spanning the Gd L_2 edge, as illustrated in Fig. 3A. The sign and magnitude of F_{cir} vary rapidly as a function of photon energy, with comparatively low magnetic contrast for photon energies far from the resonance, i.e., at 7.932 and 7.946 keV. The energy dependence of the flipping ratio F_{cir} predicted using the FDMNES package is shown in Fig. 3B, assuming the Gd magnetization pointing along the cubic ⟨111⟩ directions (*31*). The predicted values of F_{cir} reach a relative maximum near 7.940 keV, with a strong dependence on the direction of the Gd magnetization. With the assumption that the probed area has the bulk magnetic structure with magnetic easy directions along ⟨111⟩, large positive and negative values of F_{cir} are expected for magnetizations along [111] and [$\bar{1}\,\bar{1}$1] (or [11$\bar{1}$] and [$\bar{1}\,\bar{1}\,\bar{1}$]) because these directions lie within the plane containing the incident and diffracted x-ray beams (*28*).

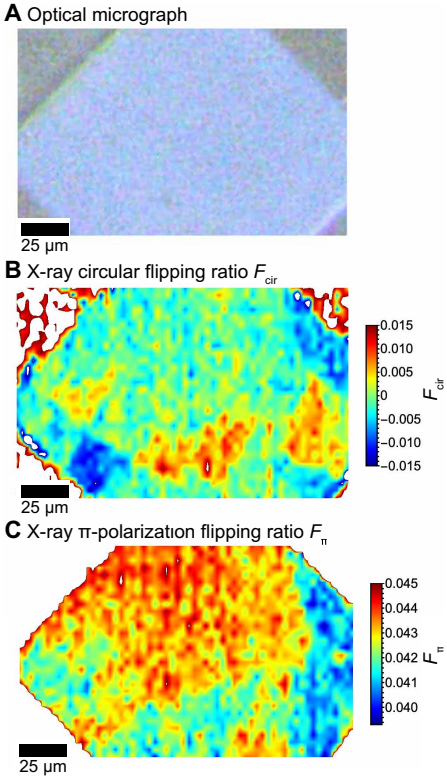

Fig. 2. Domain imaging in GdIG SSE devices. (**A**) Optical micrograph of a patterned GdIG layer from which GdIG has been removed in the area outside the light square. X-ray nanobeam diffraction maps of (**B**) circular-polarization flipping ratio F_{cir} and (**C**) linear π-polarization flipping ratio F_π in the same region. The areas of nearly uniform contrast at the edges of the images in (B) and (C) are in regions from which the GdIG layer had been removed and in which there is vanishingly low diffracted intensity.

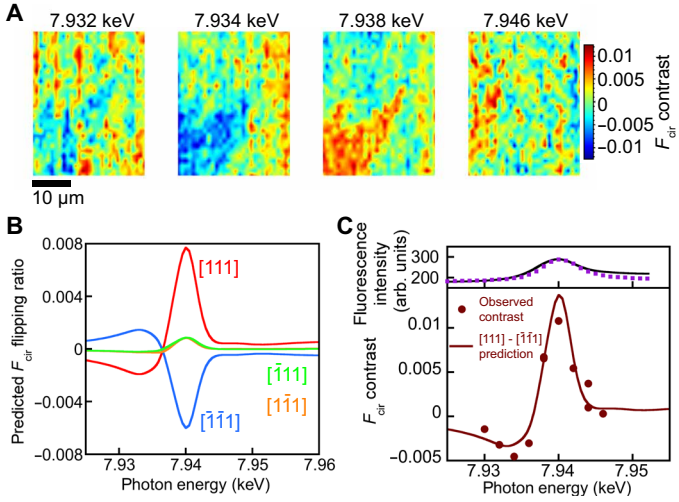

Fig. 3. X-ray photon energy dependence of resonant scattering contrast. (**A**) Maps of F_{cir} of the same region of the GdIG layer for several photon energies near the Gd L_2 resonance. (**B**) Predicted F_{cir} for four ⟨111⟩ magnetization directions. (**C**) Observed and predicted contrast of F_{cir} measured for regions of (A) with opposite values of F_{cir} (bottom). X-ray fluorescence intensity as a function of photon energy (top).

The measured magnetic contrast between domains of opposite values of F_{cir} is shown as a function of photon energy in Fig. 3C. The magnetic contrast was measured using the integrated intensities in regions at the bottom left and bottom right of the images in Fig. 3A. By comparing the predicted and observed contrasts, we identify areas with large positive and negative values of F_{cir} to be regions with [111] and [$\bar{1}\bar{1}$1] directions of the magnetization of GdIG, respectively. The maximum contrast is 1.6% at 7.940 keV. The maxima of the observed and predicted contrast agree and occur at the maximum in the total x-ray fluorescence, also shown in Fig. 3C. The close agreement between the predicted F_{cir} and fluorescence and the experimental observations of these quantities allows us to use the simulation to interpret the magnetic contrast reliably and to obtain maps of the distribution of the Gd magnetization in the GdIG thin film.

Maps of F_{cir} were acquired for a second GdIG area at a photon energy of 7.938 keV and are shown in Fig. 4A. The precision of the experiment permits the unambiguous distinction of at least three values of F_{cir} at this photon energy, corresponding to different orientations of the Gd magnetization. Comparing the measured contrast with the contrast expected based on the predicted flipping ratios with these three ranges of F_{cir}, the local orientation of the Gd magnetization within several domains can be determined to within an uncertainty of the sign of the magnetization. A diagram of the directions of the magnetic axes within the region mapped in Fig. 4A is shown in Fig. 4B.

As is apparent from both Figs. 2A and 4B, domain walls in the GdIG layer are, in some places, oriented in preferred crystallographic directions over distances of tens of micrometers. The domain boundaries in Fig. 4A have in-plane ⟨110⟩, ⟨100⟩, and approximately ⟨310⟩ orientations, and the same domain wall orientations are also apparent in regions of Figs. 2B and 3A. A detailed free energy analysis (see Materials and Methods) predicts that in (001)-oriented GdIG thin films, the shape anisotropy causes the magnetization to be along ⟨110⟩ directions, i.e., in the plane of the film rather than ⟨111⟩ as in bulk GdIG, and that the Néel walls form with a fourfold magnetic anisotropy along one of the four in-plane ⟨110⟩ directions. The magnetic contrast for the ⟨110⟩ magnetization configuration can be expected to follow the same qualitative photon energy dependence discussed above, with large magnitudes of F_{cir} observed when the magnetic moment is in the scattering plane. The calculations also show that the in-plane ⟨100⟩ boundary is expected to be a low-energy 90° Néel wall.

DISCUSSION

The fine-scale domain pattern and the distribution of domain wall directions in Fig. 2 indicate that effects beyond the domain wall energy contribute to determining the magnetic microstructure. The small-scale distribution of domain directions is further apparent in Fig. 5A, which shows three maps of F_{cir} acquired at a photon energy of 7.938 keV at different scales from a region within Fig. 2. The region imaged in Fig. 5A is identical to Fig. 3, which permits regions of high and low F_{cir} in Fig. 5A to be assigned to [111] and [$\bar{1}\,\bar{1}$1] magnetization, respectively. The domains exhibit a complex arrangement in which some regions of domain walls are clearly oriented with crystallographic facets, while others are disordered at the smallest imaged scale. Free energy calculations (see Materials and Methods) reveal that the energy degeneracy of the in-plane magnetization directions is removed because of the magnetocrystalline anisotropy and thus indicate that the domain pattern occurs within a complex energetic landscape in which domain walls also interact with a spatially complex strain field.

A structural investigation reveals that the synthesis of the GdIG epitaxial layers results in the spontaneous formation of a nanoscale

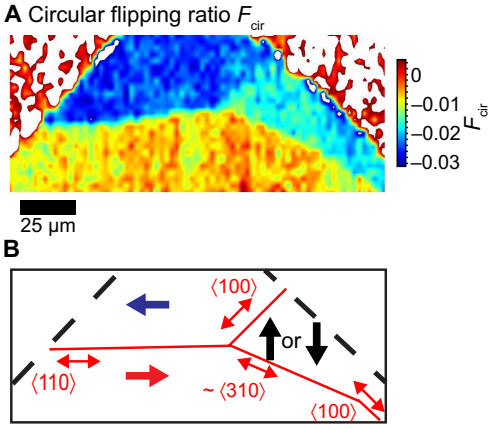

Fig. 4. Magnetic domain wall orientation and magnetic structure. (**A**) Nanobeam diffraction map of F_{cir} within a region of the GdIG pattern with large magnetic domains. The footprint of the incident and diffracted x-ray beams is horizontal. The nearly uniform contrast at the edges of the image in (A) is in regions from which the GdIG layer had been removed. (**B**) Schematic of the in-plane projection of the magnetization of the domains. The edges of the patterned GdIG layer are indicated by dashed lines.

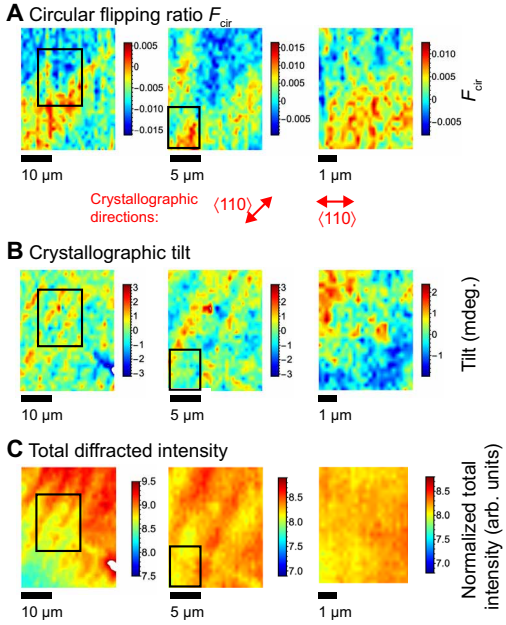

Fig. 5. Interaction between crystallographic and magnetic microstructure. (**A**) Nanobeam diffraction maps of F_{cir} at micrometer length scales. The in-plane crystallographic directions are shown in the diagram below the images. (**B**) Crystallographic tilt toward the [010] (vertical) direction. (**C**) Integrated diffracted x-ray intensity at the 008 Bragg reflection. The magnetic response to the structural variation in (B) and (C) competes with the development of facets along directions of the lowest domain boundary energy.

crystalline microstructure, as in maps of the lattice tilt along the direction of the beam footprint shown in Fig. 5B. Here, the orientation of the lattice, Fig. 5B, exhibits variations on the order of 10^{-3}° over micrometer-scale distances. Previous nanobeam studies in other epitaxial systems indicate that this tilting pattern can arise from complex series of effects including extended defects and surface steps (*32*). The tilt images and the map of the total diffracted intensity shown in Fig. 5C both span the same regions as the magnetic maps in Fig. 5A. A similar pattern of spatial variation appears in the overall diffracted intensity in Fig. 5C.

The structural results in Fig. 5 indicate that exploiting the influence of crystallographic microstructure on the domain configuration and magnetic anisotropy will make it possible to develop garnet-based devices with structurally controlled magnetism. Such approaches have previously been used at far larger length scales to tune the magnetic anisotropy in garnets, including by varying of the epitaxial mismatch between the garnet film and its substrate (*33*, *34*). It is now clear that this structural approach to the control of domain patterns is applicable at the nanoscale.

The imaging study presented here represents an important first step in combining nanometer-resolution structural and magnetic probes to address challenges in spintronics. The ability to reveal the coupling between magnetism and crystallographic structure is an important distinction between magnetic diffraction and magnetic imaging using x-ray spectroscopy. The future use of nanobeam magnetic diffraction includes the possibility of providing an additional contrast mechanism based on the incident-angle dependence of the magnetic scattering cross sections by studying different Bragg reflections. Present developments in x-ray sources provide the optical brilliance required to investigate room temperature nanoscale magnetic domains, for which exploiting the weaker magnetic resonance of the Fe resonance edge will be essential. Ptychographic analysis will permit the simultaneous and rapid reconstruction of magnetic and structural information at the nanometer scale and in three dimensions, as is presently possible with studies of the crystallographic structure (*35*). Last, combining nanobeam diffraction with time-resolved techniques, including those based at x-ray free-electron laser light sources, has the potential to open up new fields based on understanding the coupling between the dynamics of the crystal lattice, nanoscale domain patterns, and the magnetic functionality (*36*, *37*).

The magnetic structure of GdIG revealed here has potentially profound consequences for the design of materials for spintronic devices based on the SSE. The diversity of domain directions apparent in magnetic images indicates that the low–magnetic field SSE is significantly affected by the vector addition of electric fields from regions of different magnetization. The discovery of the domain morphology at zero field and the apparent interaction of the domain walls with the crystallographic distortion offer a novel way to enhance low-field SSE by optimizing the structural properties of the device. This can be done, in principle, through the selection of oxide substrates with optimized symmetry and lattice parameter and through the nanomechanical design of the SSE device. More generally, the results suggest that further opportunities will arise in the interaction of structural and magnetic effects at the nanoscale, for example, the discovery of new types of domain walls that cannot be stabilized by magnetic fields alone, analogously to the formation of charged domain walls in improper ferroelectrics.

MATERIALS AND METHODS

GdIG thin-film fabrication and characterization

GdIG has a cubic crystal structure with a large unit cell in which magnetism arises from both Fe^{3+} and Gd^{3+} ions. The Fe^{3+} ions are in inequivalent octahedral (16a) and tetrahedral (24d) sites, and Gd^{3+} ions are located at (24c) dodecahedral sites. In bulk, GdIG is ferrimagnetic, with a Curie temperature T_C = 560 K and Fe^{3+} magnetic moments on the octahedral and tetrahedral sites along opposite directions in the ⟨111⟩ family, a total of eight possible local directions of the magnetization. The difference in the number of Fe^{3+} ions on the two inequivalent sites leads to a net Fe magnetization. The Gd sublattice magnetization has a direction opposite the net Fe magnetization at zero magnetic field and has a magnitude that increases at low temperature and serves as a reliable marker of the local magnetization (*4*, *38*).

The GdIG thin film was deposited on a single crystalline, (100)-oriented gadolinium gallium garnet [$Gd_3Ga_5O_{12}$ (GGG)] substrate by pulsed laser deposition using a KrF excimer laser and a stoichiometric GdIG target. Optimized structural and magnetic properties of the GdIG thin films were obtained by using a substrate temperature of 450°C, a pure oxygen atmosphere of 25 μbar, a laser energy fluence of 2.0 J/cm^2 at the target surface, and a frequency of the excimer laser of 10 Hz. We here focus on a 21-nm-thick GdIG thin film. The high crystalline quality and low mosaicity of the GdIG layer were demonstrated by the presence of thickness fringes around the GdIG 400 reflection and by the low FWHM of the rocking curve around the 400 reflection of less than 0.02°. The GdIG had an out-of-plane lattice constant of 1.258 ± 0.002 nm, which is slightly larger than the bulk value of 1.247 nm due to the compressive in-plane strain imposed by the GGG substrate. The GdIG thin film was covered in situ, without breaking the vacuum, with a 2.8-nm-thick Pt layer deposited via electron beam evaporation at room temperature.

For the longitudinal SSE experiment, the GdIG/Pt bilayer is patterned into a Hall bar mesa structure, as shown in Fig. 1C, using optical lithography and Ar ion beam milling. A temperature gradient across the GdIG/Pt interface along the surface normal **z** was generated by sourcing a large current of 6 mA along the Hall bar in **x** direction. The longitudinal resistance of the Pt layer is exploited for on-chip thermometry. The transverse voltage V_{SSE} (along the **y** direction) was measured as a function of the magnetic field applied along the **x** direction for three different temperatures 20, 150, and 300 K. A current reversal method was used to exclude any spurious asymmetric effects (*39*).

As illustrated in Fig. 1D, V_{SSE} has opposite signs at a fixed value of $\mu_0 H$ above the magnetic saturation field for temperatures below and above the magnetic compensation temperature, T_{comp} = 288 K, at which the total remnant magnetization passes through zero due to the net cancellation of the magnetizations of the Fe and Gd sublattices. At a finite magnetic field, the direction of the total magnetization, including both the Gd and Fe sublattice reverses at T_{comp}, causing the observed sign change of V_{SSE} between 300 and 150 K. Another sign change of V_{SSE} can be observed between 150 and 20 K due to the competition of the heat-to-spin current conversion efficiency from different magnon branches (*4*, *11*).

X-ray nanobeam diffraction experimental details

X-ray nanobeam diffraction experiments were conducted at the ID01 beamline of the European Synchrotron Radiation Facility. A two-bounce horizontal deflection Si [111] monochromator produced an

incident beam with linear polarization in the horizontal plane with energy bandwidth $\Delta E/E \approx 10^{-4}$. An x-ray phase plate was added to the beamline to allow the incident polarization to be selected (*40*). A quarter-wave setting was used to convert the incident linear σ-polarized photons from the undulator insertion device to left and right circular polarized light. A second, half-wave setting was used to produce incident π-polarized light.

For the experiments described in the main text, the incident photon energy E was tuned to the Gd L_2 absorption edge near $E = 7.94$ keV to maximize the scattering sensitivity to the Gd magnetic moments via x-ray resonant scattering (*41*). The incident x-ray beam was focused to a spot on the sample using a Fresnel zone plate (FZP) with an outermost zone width of 100 nm. The beam focused to the first-order focus of the zone plate was selected with an order-sorting aperture. At the Gd L_2 edge, the Bragg angle for the GdIG 008 reflection is 30.06°. The focused beam cross section had a FWHM of 200 nm, leading to a footprint on the surface at the Bragg condition of 200 nm (along horizontal direction of the maps in Figs. 2 to 4) × 400 nm (along the vertical direction in the maps). Maps of the intensity of the GdIG 008 reflection were acquired by scanning the FZP using a piezoelectric stage. The change in the effective diffracted beam angle during the scans was orthogonal to the angle analyzed to form the tilt map shown in Fig. 5B. The sample was cooled in a continuous flow helium cryostat.

The intensity maps were repeated for incident left-, right-, and π-polarized light. The flipping ratios F_{cir} and F_π discussed in the text were computed at each pixel of the map by (i) correcting the measured diffracted intensity to remove source intensity variations by using the signal from an intensity normalization detector located before the diamond phase plate and (ii) separately correcting the left-, right-, and π-polarized signals to account for the small difference in the intensity of the x-ray beams transmitted through the phase plate at the angular settings resulting in these polarizations.

SUPPLEMENTARY MATERIALS

Supplementary material for this article is available at http://advances.sciencemag.org/cgi/content/full/6/40/eaba9351/DC1

REFERENCES AND NOTES

1. S. A. Wolf, D. D. Awschalom, R. A. Buhrman, J. M. Daughton, S. von Molnár, M. L. Roukes, A. Y. Chtchelkanova, D. M. Treger, Spintronics: A spin-based electronics vision for the future. *Science* **294**, 1488–1495 (2001).
2. S. I. Kiselev, J. C. Sankey, I. N. Krivorotov, N. C. Emley, R. J. Schoelkopf, R. A. Buhrman, D. C. Ralph, Microwave oscillations of a nanomagnet driven by a spin-polarized current. *Nature* **425**, 380–383 (2003).
3. G. E. W. Bauer, E. Saitoh, B. J. van Wees, Spin caloritronics. *Nat. Mater.* **11**, 391–399 (2012).
4. S. Geprägs, A. Kehlberger, F. Della Coletta, Z. Qiu, E.-J. Guo, T. Schulz, C. Mix, S. Meyer, A. Kamra, M. Althammer, H. Huebl, G. Jakob, Y. Ohnuma, H. Adachi, J. Barker, S. Maekawa, G. E. W. Bauer, E. Saitoh, R. Gross, S. T. B. Goennenwein, M. Kläui, Origin of the spin Seebeck effect in compensated ferrimagnets. *Nat. Commun.* **7**, 10452 (2016).
5. G. J. Snyder, E. S. Toberer, Complex thermoelectric materials. *Nat. Mater.* **7**, 105–114 (2008).
6. R. Venkatasubramanian, E. Siivola, T. Colpitts, B. O'Quinn, Thin-film thermoelectric devices with high room-temperature figures of merit. *Nature* **413**, 597–602 (2001).
7. K. Uchida, S. Takahashi, K. Harii, J. Ieda, W. Koshibae, K. Ando, S. Maekawa, E. Saitoh, Observation of the spin Seebeck effect. *Nature* **455**, 778–781 (2008).
8. K.-i. Uchida, T. Nonaka, T. Ota, E. Saitoh, Longitudinal spin-Seebeck effect in sintered polycrystalline (Mn, Zn) Fe_2O_4. *Appl. Phys. Lett.* **97**, 262504 (2010).
9. J. Xiao, G. E. W. Bauer, K.-i. Uchida, E. Saitoh, S. Maekawa, Theory of magnon-driven spin Seebeck effect. *Phys. Rev. B* **81**, 214418 (2010).
10. E. Saitoh, M. Ueda, H. Miyajima, G. Tatara, Conversion of spin current into charge current at room temperature: Inverse spin-Hall effect. *Appl. Phys. Lett.* **88**, 182509 (2006).
11. J. Cramer, E.-J. Guo, S. Geprägs, A. Kehlberger, Y. P. Ivanov, K. Ganzhorn, F. Della Coletta, M. Althammer, H. Huebl, R. Gross, J. Kosel, M. Kläui, S. T. B. Goennenwein, Magnon mode selective spin transport in compensated ferrimagnets. *Nano Lett.* **17**, 3334–3340 (2017).
12. I. Gray, T. Moriyama, N. Sivadas, G. M. Stiehl, J. T. Heron, R. Need, B. J. Kirby, D. H. Low, K. C. Nowack, D. G. Schlom, D. C. Ralph, T. Ono, G. D. Fuchs, Spin Seebeck imaging of spin-torque switching in antiferromagnetic Pt/NiO heterostructures. *Phys. Rev. X* **9**, 041016 (2019).
13. J. F. K. Cooper, C. J. Kinane, S. Langridge, M. Ali, B. J. Hickey, T. Niizeki, K. Uchida, E. Saitoh, H. Ambaye, A. Glavic, Unexpected structural and magnetic depth dependence of YIG thin films. *Phys. Rev. B* **96**, 104404 (2017).
14. J. Mendil, M. Trassin, Q. Bu, J. Schaab, M. Baumgartner, C. Murer, P. T. Dao, J. Vijayakumar, D. Bracher, C. Bouillet, C. A. F. Vaz, M. Fiebig, P. Gambardella, Magnetic properties and domain structure of ultrathin yttrium iron garnet/Pt bilayers. *Phys. Rev. Mater.* **3**, 034403 (2019).
15. M. Kubota, A. Tsukazaki, F. Kagawa, K. Shibuya, Y. Tokunaga, M. Kawasaki, Y. Tokura, Stress-induced perpendicular magnetization in epitaxial iron garnet thin films. *Appl. Phys. Exp.* **5**, 103002 (2012).
16. A. M. Kalashnikova, V. V. Pavlov, A. V. Kimel, A. Kirilyuk, T. Rasing, R. V. Pisarev, Magneto-optical study of holmium iron garnet $Ho_3Fe_5O_{12}$. *Low Temp. Phys.* **38**, 863–869 (2012).
17. R. W. Hansen, L. E. Helseth, A. Solovyev, E. Il'Yashenko, T. H. Johansen, Growth and characterization of (100) garnets for imaging. *J. Magnet. Magnet. Mater.* **272-276**, 2247–2249 (2004).
18. P. G. Evans, E. D. Isaacs, G. Aeppli, Z. Cai, B. Lai, X-ray microdiffraction images of antiferromagnetic domain evolution in chromium. *Science* **295**, 1042–1045 (2002).
19. T. Higo, H. Man, D. B. Gopman, L. Wu, T. Koretsune, O. M. J. van't Erve, Y. P. Kabanov, D. Rees, Y. Li, M.-T. Suzuki, S. Patankar, M. Ikhlas, C. L. Chien, R. Arita, R. D. Shull, J. Orenstein, S. Nakatsuji, Large magneto-optical Kerr effect and imaging of magnetic octupole domains in an antiferromagnetic metal. *Nat. Photonics* **12**, 73–78 (2018).
20. J. Li, J. Pelliciari, C. Mazzoli, S. Catalano, F. Simmons, J. T. Sadowski, A. Levitan, M. Gibert, E. Carlson, J.-M. Triscone, S. Wilkins, R. Comin, Scale-invariant magnetic textures in the strongly correlated oxide $NdNiO_3$. *Nat. Commun.* **10**, 4568 (2019).
21. S.-W. Cheong, M. Fiebig, W. Wu, L. Chapon, V. Kiryukhin, Seeing is believing: Visualization of antiferromagnetic domains. *npj Quantum Mater.* **5**, 3 (2020).
22. M. Seul, L. R. Monar, L. O'Gorman, R. Wolfe, Morphology and local structure in labyrinthine stripe domain phase. *Science* **254**, 1616–1618 (1991).
23. H. Maier-Flaig, S. Geprägs, Z. Qiu, E. Saitoh, R. Gross, M. Weiler, H. Huebl, S. T. B. Goennenwein, Perpendicular magnetic anisotropy in insulating ferrimagnetic gadolinium iron garnet thin films. arXiv:1706.08488 [cond-mat.mtrl-sci] (2017).
24. E. R. Rosenberg, L. Beran, C. O. Avci, C. Zeledon, B. Song, C. Gonzalez-Fuentes, J. Mendil, P. Gambardella, M. Veis, C. Garcia, G. S. D. Beach, C. A. Ross, Magnetism and spin transport in rare-earth-rich epitaxial terbium and europium iron garnet films. *Phys. Rev. Mater.* **2**, 094405 (2018).
25. S. B. Ubizskii, Orientational states of magnetization in epitaxial (111)-oriented iron garnet films. *J. Magnet. Magnet. Mater.* **195**, 575–582 (1999).
26. S. M. Aliev, I. K. Kamilov, M. S. Aliev, Z. G. Ibaev, A study of the domain structure of ferrites in the vicinity of the compensation point by Mössbauer spectroscopy. *Tech. Phys. Lett.* **42**, 118–120 (2016).
27. T. Yoshimoto, T. Goto, K. Shimada, B. Iwamoto, Y. Nakamura, H. Uchida, C. A. Ross, M. Inoue, Static and dynamic magnetic properties of single-crystalline yttrium iron garnet films epitaxially grown on three garnet substrates. *Adv. Electron. Mater.* **4**, 1800106 (2018).
28. D. Haskel, E. Kravtsov, Y. Choi, J. C. Lang, Z. Islam, G. Srajer, J. S. Jiang, S. D. Bader, P. C. Canfield, Charge-magnetic interference resonant scattering studies of ferromagnetic crystals and thin films. *Euro. Phys. J. Spec. Top.* **208**, 141–155 (2012).
29. Y. Sasaki, M. Okube, S. Sasaki, Resonant and non-resonant magnetic scatterings with circularly polarized x-rays: Magnetic scattering factor and electron density of gadolinium iron garnet. *Acta Cryst. A* **73**, 257–270 (2017).
30. C. Donnelly, M. Guizar-Sicairos, V. Scagnoli, S. Gliga, M. Holler, J. Raabe, L. J. Heyderman, Three-dimensional magnetization structures revealed with x-ray vector nanotomography. *Nature* **547**, 328–331 (2017).
31. O. Bunău, Y. Joly, Self-consistent aspects of x-ray absorption calculations. *J. Phys. Condens. Matter* **21**, 345501 (2009).
32. P. G. Evans, D. E. Savage, J. R. Prance, C. B. Simmons, M. G. Lagally, S. N. Coppersmith, M. A. Eriksson, T. U. Schulli, Nanoscale distortions of Si quantum wells in Si/SiGe quantum-electronic heterostructures. *Adv. Mater.* **24**, 5217–5221 (2012).
33. E. A. Giess, D. C. Cronemeyer, Magnetic anisotropy of $Eu_{0.65}Y_{2.35}Fe_{3.8}Ga_{1.2}O_{12}$ films grown on garnet substrates with different lattice parameters. *Appl. Phys. Lett.* **22**, 601–602 (1973).
34. J. Fu, M. Hua, X. Wen, M. Xue, S. Ding, M. Wang, P. Yu, S. Liu, J. Han, C. Wang, H. Du, Y. Yang, J. Yang, Epitaxial growth of $Y_3Fe_5O_{12}$ thin films with perpendicular magnetic anisotropy. *Appl. Phys. Lett.* **110**, 202403 (2017).

35. P. Godard, G. Carbone, M. Allain, F. Mastropietro, G. Chen, L. Capello, A. Diaz, T. H. Metzger, J. Stangl, V. Chamard, Three-dimensional high-resolution quantitative microscopy of extended crystals. *Nat. Commun.* **2**, 568 (2011).
36. K. Shen, Temperature-switched anomaly in the spin Seebeck effect in $Gd_3Fe_5O_{12}$. *Phys. Rev. B* **99**, 024417 (2019).
37. C. O. Avci, E. Rosenberg, L. Caretta, F. Büttner, M. Mann, C. Marcus, D. Bono, C. A. Ross, G. S. D. Beach, Interface-driven chiral magnetism and current-driven domain walls in insulating magnetic garnets. *Nat. Nanotechnol.* **14**, 561–566 (2019).
38. H. Miyagawa, N. Kawamura, M. Suzuki, Temperature dependence of x-ray magnetic circular dichroism in rare earth iron garnets (rare earth = Gd, Dy and Sm). *Phys. Scr.* **2005**, 616 (2005).
39. M. Schreier, N. Roschewsky, E. Dobler, S. Meyer, H. Huebl, R. Gross, S. T. B. Goennenwein, Current heating induced spin Seebeck effect. *Appl. Phys. Lett.* **103**, 242404 (2013).
40. J. C. Lang, G. Srajer, Bragg transmission phase plates for the production of circularly polarized x-rays. *Rev. Sci. Instrum.* **66**, 1540–1542 (1995).
41. J. C. Lang, X. Wang, V. P. Antropov, B. N. Harmon, A. I. Goldman, H. Wan, G. C. Hadjipanayis, K. D. Finkelstein, Circular magnetic x-ray dichroism in crystalline and amorphous $GdFe_2$. *Phys. Rev. B* **49**, 5993–5998 (1994).
42. M. Suzuki, Y. Inubushi, M. Yabashi, T. Ishikawa, Polarization control of an X-ray free-electron laser with a diamond phase retarder. *J. Synchrotron Rad.* **21**, 466–472 (2014).
43. S. Geprägs, A. Brandlmaier, M. S. Brandt, R. Gross, S. T. B. Goennenwein, Strain-controlled nonvolatile magnetization switching. *Solid State Commun.* **198**, 7–12 (2014).
44. B. A. Calhoun, M. J. Freiser, Anisotropy of gadolinium iron garnet. *J. Appl. Phys.* **34**, 1140–1145 (1963).
45. R. L. Comstock, J. J. Raymond, W. G. Nilsen, J. P. Remeika, Spin-wave spectrum of gadolinium iron garnet. *Appl. Phys. Lett.* **9**, 274–276 (1966).
46. A. E. Clark, J. J. Rhyne, E. R. Callen, Magnetostriction of dilute dysprosium iron and of gadolinium iron garnets. *J. Appl. Phys.* **39**, 573–575 (1968).
47. N. A. Pertsev, Giant magnetoelectric effect via strain-induced spin reorientation transitions in ferromagnetic films. *Phys. Rev. B* **78**, 212102 (2008).
48. J.-M. Hu, C. W. Nan, Electric-field-induced magnetic easy-axis reorientation in ferromagnetic/ferroelectric layered heterostructures. *Phys. Rev. B* **80**, 224416 (2009).
49. M. Weiler, A. Brandlmaier, S. Geprägs, M. Althammer, M. Opel, C. Bihler, H. Huebl, M. S. Brandt, R. Gross, S. T. B. Goennenwein, Voltage controlled inversion of magnetic anisotropy in a ferromagnetic thin film at room temperature. *New J. Phys.* **11**, 013021 (2009).
50. B. D. Cullity, C. D. Graham, *Introduction to Magnetic Materials* (John Wiley & Sons, 2011).

Acknowledgments: We thank the staff of XMaS (BM28), the UK-CRG beamline at the ESRF for lending the diamond phase plate. We also thank D. Haskel of the Argonne National Laboratory for useful discussions and gratefully acknowledge the staff of the ESRF ID01 beamline for support during the experiment. **Funding:** P.G.E. and S.D.M. acknowledge support from the U.S. Department of Energy Office of Basic Energy Sciences through contract DE-FG02-04ER46147. S.D.M. acknowledges travel support from the NSF through the University of Wisconsin Materials Research Science and Engineering Center through grant number DMR-1720415. S.G. and R.G. acknowledge financial support of the German Research Foundation via Germany's Excellence Strategy (EXC-2111-390814868). **Author contributions:** D.M., D.C., and P.G.E. conceived the experiment. S.D.M., D.M., P.G.E., S.G., and T.U.S. conducted the x-ray nanobeam diffraction study. S.D.M., D.M., P.G.E., M.-I.R., and D.C. analyzed the nanodiffraction results. P.B.J.T. and L.B. designed and implemented the x-ray phase plate x-ray polarizer. Y.J. simulated the resonant scattering magnetic contrast. S.G., M. Dietlein, and R.G. synthesized the GdIG thin films and conducted magnetic, spin caloritronic, and structural characterization. M. Dai and J.H. implemented and analyzed the free energy analysis and domain wall energy calculations. **Competing interests:** The authors declare that they have no competing interests. **Data and materials availability:** All data needed to evaluate the conclusions in the paper are present in the paper and/or the Supplementary Materials. Additional data related to this paper may be requested from the authors.

Submitted 17 January 2020
Accepted 19 August 2020
Published 2 October 2020
10.1126/sciadv.aba9351

Citation: P. G. Evans, S. D. Marks, S. Geprägs, M. Dietlein, Y. Joly, M. Dai, J. Hu, L. Bouchenoire, P. B. J. Thompson, T. U. Schülli, M.-I. Richard, R. Gross, D. Carbone, D. Mannix, Resonant nanodiffraction x-ray imaging reveals role of magnetic domains in complex oxide spin caloritronics. *Sci. Adv.* **6**, eaba9351 (2020).